ACS APPLIED MATERIALS & INTERFACES

Research Article

www.acsami.org

Comparative Investigation of Phosphate-Based Composite Cathode Materials for Lithium-Ion Batteries

Jun-chao Zheng,† Ya-dong Han,† Bao Zhang,* Chao Shen, Lei Ming, and Jia-feng Zhang

School of Metallurgy and Environment, Central South University, Changsha 410083, P.R. China

ABSTRACT: $Li_3V_2(PO_4)_3$–$LiVPO_4F$, $LiFePO_4$–$Li_3V_2(PO_4)_3$, and $LiFePO_4$–$Li_3V_2(PO_4)_3$–$LiVPO_4F$ composite cathode materials are synthesized through mechanically activated chemical reduction followed by annealing. X-ray diffraction (XRD) results reveal that the obtained products are pure phase, and the molar ratio of each phase in the composites is consistent with that in raw material. Transmission electron microscopy (TEM) images show that each phase coexists in the composites. The $LiFePO_4$–$Li_3V_2(PO_4)_3$–$LiVPO_4F$ composites exhibit the best electrochemical performance. These composites can deliver a capacity of 164 mAh g^{-1} at 0.1 C and possess favorable capacities at rates of 0.5, 1, and 5 C. The excellent electrochemical performance is attributed to the mutual modification and the synergistic effects.

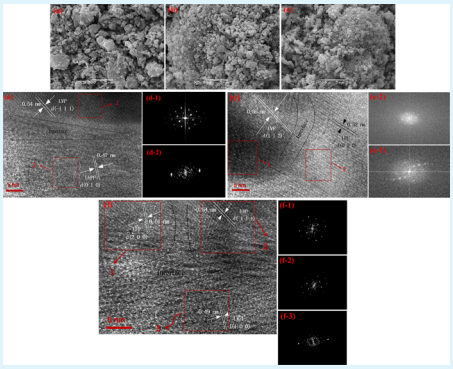

KEYWORDS: *lithium-ion battery, phosphate-based cathode material, electrochemical performance, mutual modification, synergistic effects*

1. INTRODUCTION

Since first presented by Rustum Roy in 1984, nanocomposites have attracted considerable attention in the material fields.[1] When two or more materials with different advantages and performances form a composite material, the synergy among the various components produces a variety of complex effects and generates complementary advantages. Therefore, obtaining a composite material with better performance in terms of its physical, chemical, or mechanical properties by using the "synergistic effects" can be expected.[2−4] Recently, numerous researchers have attempted to synthesize composite materials for lithium ion batteries, and their results indicate that the composite materials have significantly better electrochemical performances than bare batteries.[5−13]

Phosphate-based cathode materials for $LiFePO_4$[14,15] and $Li_3V_2(PO_4)_3$,[16] which undergo a two-phase insertion reaction, limit the rate capability when the particles are extremely large. For $LiMnPO_4$,[17] synthesizing the sample with electrochemical activity is difficult, and the dissolution of Mn limits its cycle performance. For $LiVPO_4F$,[18,19] synthesizing the high pure phase is difficult, and the low electronic conductivity limits the electrochemical performance. The slow kinetics limit the application of phosphate-based cathode materials. Various strategies, such as carbon coating, use of nanoparticles, and metal doping, have been reported to solve the problem.[20−24] However, these methods all have their disadvantages, such as that carbon coating will result in a low tap density and energy density of the materials. Nanostructure cathode materials require a special design of the synthesis strategy and complex synthetic techniques. Besides, these methods can only improve some properties, such as the improvement of electronic conductivity for carbon coating, shorten Li^+ transport distance, and quicken Li-ion diffusion for the nanoparticle. The partial improvement is not enough, and the nonuniform carbon coating and nanoparticle morphology and inaccurate doping location also limit the improvement of slow kinetics for the phosphate-based cathode materials. Thus, it needs a more effective method to improve the electrochemical properties including the capacity, rate, and cycle performance of the cathode material. Recently, that synthesizing composite materials for lithium ion batteries is a good proposal to improve the electrochemical properties of the cathode material has been reported.[12,25−28] The composite materials can make full use of the advantages for each phase and new synergistic effects between them. Our group and other researchers have synthesized several phosphate-based polyanionic composite cathode materials (mainly focused on two-phase composites, such as $LiFePO_4$–$Li_3V_2(PO_4)_3$, $Li_3V_2(PO_4)_3$–$LiVPO_4F$, and $LiFePO_4$–$LiVPO_4F$) and studied their properties.[29−34] The results of these studies show that the composite materials have better electrochemical performance than that of single-phase material.

In this study, we attempted to synthesize a two-phase composite $Li_3V_2(PO_4)_3$–$LiVPO_4F$ and $LiFePO_4$–$Li_3V_2(PO_4)_3$ and a three-phase composite $LiFePO_4$–$Li_3V_2(PO_4)_3$–$LiVPO_4F$, and their performances are comparatively investigated.

Received: April 29, 2014
Accepted: August 4, 2014
Published: August 4, 2014

   dx.doi.org/10.1021/am502601r | ACS Appl. Mater. Interfaces 2014, 6, 13520−13526

2. EXPERIMENTAL SECTION

The composites are synthesized by mechanically activated chemical reduction followed by annealing. The $LiFePO_4$, $Li_3V_2(PO_4)_3$, and $LiVPO_4F$ are marked as LFP, LVP, and LVPF, respectively.

2.1. Synthesis of the LVP−LVPF Sample. First, stoichiometric amounts of V_2O_5 (AR, ≥99.0%), LiF (AR, ≥99.0%), $LiOH·H_2O$ (AR, ≥99.0%), $NH_4H_2PO_4$, (AR, ≥99.0%), and citrate (AR, ≥99.0%) were mixed into alcohol, ball milled for 4 h, and then dried in the oven at 80 °C for 6 h to obtain a yellow amorphous precursor. Second, the dried precursor was sintered at 650 °C for 5 min in argon atmosphere to get LVP−LVPF composites. The mole ratio of LVP:LVPF is adjusted to 10:1 by controlling the weight of raw material.

2.2. Synthesis of the LFP−LVP Sample. Stoichiometric amounts of V_2O_5 (AR, ≥99.0%), $FePO_4·4H_2O$ (AR, ≥99.0%), $LiOH·H_2O$ (AR, ≥99.0%), $NH_4H_2PO_4$ (AR, ≥99.0%), and citrate (AR, ≥99.0%) were mixed into alcohol, ball milled for 4 h, and then dried in the oven at 80 °C for 6 h to obtain a yellow amorphous precursor. Second, the dried precursor was sintered at 750 °C for 8 h in argon atmosphere to get LFP−LVP composites. The mole ratio of LFP:LVP is adjusted to 6:10 by controlling the weight of raw material.

2.3. Synthesis of the LFP−LVP−LVPF Sample. Stoichiometric amounts of V_2O_5 (AR, ≥99.0%), $FePO_4·4H_2O$ (AR, ≥99.0%), LiF (AR, ≥99.0%), $LiOH·H_2O$ (AR, ≥99.0%), $NH_4H_2PO_4$ (AR, ≥99.0%), and citrate (AR, ≥99.0%) were mixed into alcohol, ball milled for 4 h, and then dried in the oven at 80 °C for 6 h to obtain a yellow amorphous precursor. Second, the dried precursor was sintered at 700 °C for 8 h in an argon atmosphere to get LFP−LVP−LVPF composites. The mole ratio of LFP:LVP:LVPF is adjusted to 6:10:1 by controlling the weight of raw material.

2.4. Structural and Morphological Characterization. Powder X-ray diffraction (XRD) (Rint-2000, Rigaku) measurements using Cu Kα radiation were utilized to identify the crystalline phases of the synthesized materials. The samples were observed using a scanning electron microscope (SEM; JEOL, JSM-5600LV) and a Tecnai G12 transmission electron microscope (TEM).

2.5. Electrochemical Measurements. Electrochemical characterization was performed using a CR2025 coin-type cell. Typical positive electrode loadings ranged from 2−2.5 mg/cm^2, and an electrode with a diameter of 14 mm was used. For positive electrode fabrication, the prepared powders were mixed with 10% carbon black and 10% polyvinylidene fluoride in *N*-methylpyrrolidinone until a slurry was obtained. The blended slurries were then pasted onto an aluminum current collector, and the electrode was dried at 120 °C for 12 h in Ar. The test cell consisted of the positive electrode and a lithium foil negative electrode separated using a porous polypropylene film and 1 mol/L $LiPF_6$ in EC, EMC, and DMC (1:1:1 v/v/v) as the electrolyte. Cell assembly was carried out in a dry Ar-filled glovebox. Electrochemical tests were conducted using an automatic galvanostatic charge−discharge unit and LAND battery cycler. The cyclic voltammetric measurements and EIS were carried out with a CHI660D electrochemical analyzer. The CV curves for the test cells were recorded at a scan rate of 0.1 mV s^{-1} in the potential range of 3.0−4.5 V. The impedance spectra were recorded by applying an AC voltage of 5 mV amplitude in the 100 KHz−0.1 Hz frequency range.

3. RESULTS AND DISCUSSION

Figure 1 shows the X-ray diffraction (XRD) patterns of the synthesized composites. The mass content of each phase in composites is obtained through Rietveld refinement (Table 1). Figure 1a shows the XRD pattern of the LVP−LVPF sample, which indicates that the synthesized powders are composed of monoclinic $Li_3V_2(PO_4)_3$ and triclinic $LiVPO_4F$ without impurities. The mole ratio of LVP:LVPF is about 10:1.02, which is near the theoretical ratio (10:1) of the raw materials. Figure 1b shows the XRD pattern of the LFP−LVP sample. The figure shows that all main peaks can be indexed to the olivine structure of $LiFePO_4$ and monoclinic $Li_3V_2(PO_4)_3$. The mole ratio of LFP:LVP is 5.95:10, which is similar to that of the raw materials. Figure 1c shows the XRD patterns of the LFP−LVP−LVPF sample, which indicates that the powders are composed of olivine $LiFePO_4$, monoclinic $Li_3V_2(PO_4)_3$, and triclinic $LiVPO_4F$. The $LiVPO_4F$ crystals grow only along the (100) planes at 18.2°, covering the (021) planes of $Li_3V_2(PO_4)_3$ at 17.9°. The $LiVPO_4F$ crystals grow only along the (100) planes because of the emerging LFP in the composites. Table 1 shows that the mole ratio of LFP:LVP:LVPF is about 5.96:10:0.91. The LVPF amount is slightly lower than in the theoretical values because of the VF_3 sublimation loss during the synthesis.[33,35] Table 2 presents the refined cell parameters of LFP, LVP, and LVPF in the synthesized samples. The LFP and LVP cell parameters in all the samples are significantly close to those reported in the literature.[29−32] The calculated lattice parameters of LVPF in the LVP−LVPF sample match well with those reported by Barker et al.[19] However, the lattice parameters of LVPF in the LFP−LVP−LVPF sample are smaller than those in the LVP−LVPF sample, as shown in Table 2c. These smaller values are caused by the preferential growth of a single crystal surface of the LVPF in the LFP−LVP−LVPF composites.

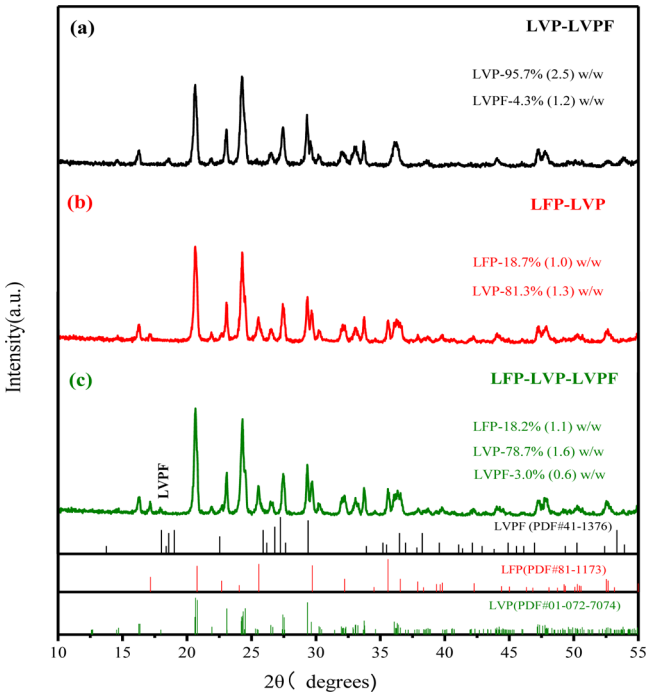

Figure 1. XRD patterns for (a) LVP−LVPF; (b) LFP−LVP; and (c) LFP−LVP−PVPF.

Table 1. Components of the Synthesized Samples

sample	mass content of LFP/LVP/LVPF (%)	mole ratio of LFP/LVP/LVPF
LVP−LVPF	0:95.7:4.3	0:10:1.02
LFP−LVP	18.7:81.3:0	5.95:10:0
LFP−LVP−LVPF	18.2:78.8:3.0	5.96:10:0.91

Figure 2 shows the SEM and TEM images of the synthesized composites. The images show that all LVP−LVPF, LFP−LVP, and LFP−LVP−LVPF powders have uniform morphologies with particle size distribution ranging from 0.5−2.0 μm. Figure 2d shows the obvious interface between $Li_3V_2(PO_4)_3$ and $LiVPO_4F$. Figure 2d-1,d-2 shows the Fourier transform (FFT) images of the selected areas. The FFT images of regions (d-1)

Table 2. Refined Unit Cell Lattice Parameters for (a) LVP−LVPF; (b) LFP−LVP; and (c) LFP−LVP−LVPF

(a) Agreement Factors R_p (%) = 8.8 in Samples						
	lattice parameters					
phase	*a*	*b*	*c*	*A*	*β*	*γ*
LFP						
LVP	8.60558	12.04229	8.59647	90	90.4894	90
LVPF	5.13823	5.4461	7.33006	65.8598	67.2586	81.7489
(b) Agreement Factors R_p (%) = 6.47 in Samples						
	lattice parameters					
phase	*a*	*b*	*C*	*α*	*β*	*γ*
LFP	10.31353	5.98564	4.69439	90	90	90
LVP	8.59852	12.0333	8.59094	90	90.5357	90
LVPF						
(c) Agreement Factors R_p (%) = 9.13 in Samples						
	lattice parameters					
phase	*a*	*b*	*c*	*A*	*β*	*γ*
LFP	10.31344	5.99779	4.69638	90	90	90
LVP	8.60534	12.03513	8.59362	90	90.5721	90
LVPF	5.10712	5.27656	7.34172	67.4085	67.4163	81.0139

and (d-2) show the $Li_3V_2(PO_4)_3$ and $LiVPO_4F$ diffraction spots, respectively. Two types of lattice fringes are found in composites (Figure 2d): first is the $Li_3V_2(PO_4)_3$ lattice fringe with an interplanar spacing of 0.54 nm and corresponds to the $(\bar{1}11)$ lattice planes, and second is the of $LiVPO_4F$ lattice fringe with an interplanar spacing of 0.47 nm and corresponds to the (010) lattice plane. The results indicate that the LVP and LVPF unit cells coexist in the composite material.

Two types of lattice fringes in the composite LFP−LVP can be also observed in Figure 2e. First is the $Li_3V_2(PO_4)_3$ lattice fringe with an interplanar spacing of 0.36 nm that corresponds to the (112) lattice planes. Second is the $LiFePO_4$ lattice fringe with an interplanar spacing of 0.52 nm that corresponds to the (020) lattice plane. The results also indicate that the LVP and LFP unit cells coexist in the composite material. The results are the same as those reported in the literature.[29,30]

The LFP lattice fringe with an interplanar spacing of 0.51 nm corresponds to the (200) lattice planes, as shown in region 1 of Figure 2f. In addition, the LVP lattice fringe with an interplanar spacing of 0.54 nm corresponds to the (111) lattice planes, as shown in region 2 of Figure 2f. Moreover, the LVPF lattice fringe with interplanar spacing of about 0.49 nm corresponds to the (100) lattice planes, which are the only lattice planes of LVPF observed in the XRD patterns, as shown in region 3 of Figure 2f. The FFT images of regions (f-1, f-2, and f-3) show the diffraction spots of $LiFePO_4$, $Li_3V_2(PO_4)_3$, and $LiVPO_4F$, respectively. The results show that LFP, LVP, and LVPF coexist in the composite. Different phases have equal opportunity for crystalline growth, and the preferential crystal plane may be influenced by the other phases.

The first charge/discharge curves for LVP−LVPF cells at 0.1C are shown in Figure 3a. It can be seen that the LVP−LVPF cell exhibits three pair charge/discharge plateaus of LVP (around 3.6 V/3.53 V, 3.7 V/3.63 V, 4.1 V/4.01 V) and a typical two steps to deintercalation and one step to intercalation Li^+ for LVPF (around 4.35 V, 4.27 V/4.14 V).[16,18−20,23] The initial discharge capacity of LVP−LVPF samples is 129.1 mAh g^{-1} at 0.1C, 95.6% of its theoretical capacity. From Figure 3d (the horizontal distance between point A and B), it can be seen that LVPF delivers a specific capacity about 15 mAh g^{-1}, 11% of the actual capacity for the composites, which is close to theoretical proportion of 10.6%. From Figure 4a, it can be seen that the LVP−LVPF composites deliver a capacity of 123.8 mAh g^{-1}, 121.1 mAh g^{-1}, and 112.3 mAh g^{-1} at higher rates of 0.5C, 1C, and 5C, respectively, and the capacity holds well with the increase of cycle and rate, which is better than that of the single LVP or LVPF phase.[16,18−21] The excellent electrochemical performance is attributed to the mutual modification between LVPF and LVP, which make full use of the high capacity, stable structure of LVPF, and 3-D fast ion transport of LVP.[19,35−38] The mutual modification composites produce a synergy between LVP and LVPF. The synergistic effect refers to that the F doping can expand the lattice of $Li_3V_2(PO_4)_3$ because of the strong inductive effect of fluorine on the PO_4^{3-} polyanion, and it can also improve electronic transmission performance of the material during charge/discharge process.[39−41] Besides, the addition of fluorine can also prevent electrode from being attacked by HF found in electrolyte and, therefore, bring about good cycle performance.[39,40] On the other hand, as the fast ionic conductor, $Li_3V_2(PO_4)_3$ possesses good Li^+ intercalation/deintercalation reversibility.

Figure 3b shows the first charge/discharge curves for LFP−LVP cells at 0.1C. The charge/discharge plateaus of LFP are at 3.49 V/3.35 V and those of LVP are at 3.6 V/3.53 V, 3.7 V/3.61 V, and 4.1 V/4.0 V. The LFP−LVP composites deliver an initial discharge capacity of 136 mAh g^{-1}, which is 91.8% of its theoretical capacity. Figure 4b shows that the LFP−LVP composites deliver a capacity of 129.4, 116.5, and 98.6 mAh g^{-1} at higher rates of 0.5, 1, and 5 C, respectively. In addition, the cycle performance of LFP−LVP composites is not as good as that of the LVP−LVPF composites. These findings can be attributed to the absence of LVPF, considering that LVPF can cause good cycle performance.

Figure 3c shows the first charge/discharge curves for LFP−LVP−LVPF cells at 0.1 C. The evident charge/discharge plateaus of LFP (at 3.5 V/3.32 V) and LVP (at 3.6 V/3.5 V, 3.7 V/3.6 V, and 4.1 V/4.0 V) are consistent with that in the LFP−LVP composites. However, only a single LVPF charge plateau is found at 4.35 V, and the corresponding discharge plateau is

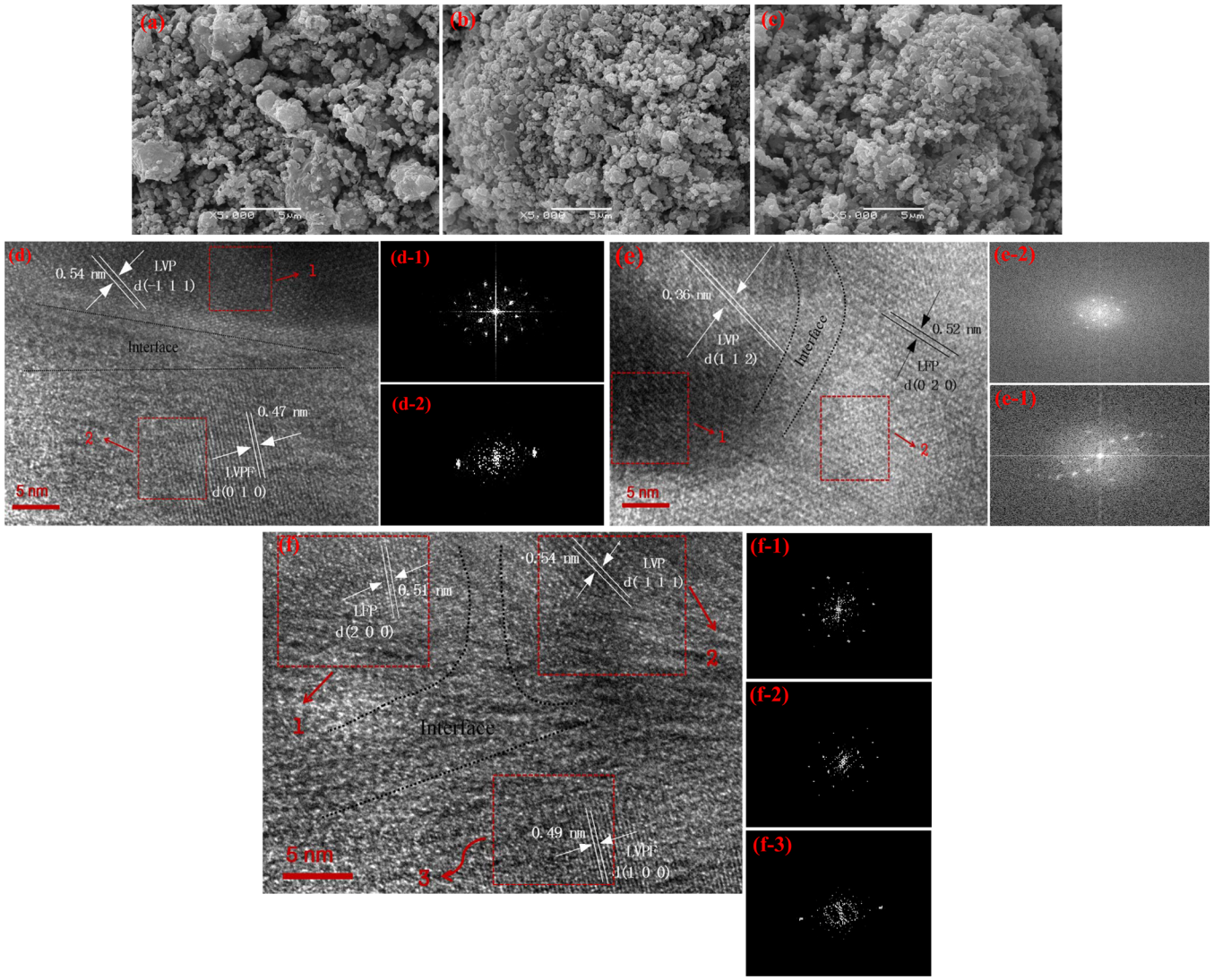

Figure 2. (a, b, c) SEM images of LVP−LVPF, LFP−LVP, LFP−LVP−LVPF; (d, e, f) TEM images of LVP−LVPF, LFP−LVP, LFP−LVP−LVPF; (d-1, d-2) Fourier transform (FFT) images of LVP−LVPF; (e-1, e-2) Fourier transform (FFT) images of LFP−LVP; (f-1, f-2, f-3) Fourier transform (FFT) images of LFP−LVP−LVPF.

not evident but is existing (as shown in Figure 3d), which is different from the bare LVPF and LVP−LVPF composites.[18,19,23] These findings may be attributed to the only (100) single LVPF crystal surface in the composites, which leads to the only insertion/deinsertion site for Li^+ of LVPF in the composites. The initial discharge capacity of LFP−LVP−LVPF composites is 164 mAh g^{-1} at 0.1 C, which is 110% of its theoretical capacity. Figure 3d shows that the LVPF discharge capacity is about 9 mAh g^{-1} (the horizontal distance between point B and C), which is 5.4% of the composites' actual capacity and is near the theoretical proportion of 5.7%. The LVP discharge capacity is about 115 mAh g^{-1}, which is 70% of the actual capacity in LFP−LVP−LVPF composites and is higher than the theoretical proportion of 52.9%. Although this phenomenon is very interesting, the reason behind it is still unclear.

Figure 4c shows the cycle and rate performance of the LFP−LVP−LVPF composites. The figure shows that the LFP−LVP−LVPF composites deliver a capacity of 156.8, 150.4, and 139 mAh g^{-1} at higher rates of 0. 5, 1, and 5 C, respectively, which is significantly better than that of the LVP−LVPF and LFP−LVP composites. The LFP−LVPF composites have been reported by Lin.[34] From the literature, the 0.99 LFP·0.01LVPF composite exhibits the best discharge capacity in a series of xLFP·(1 − x)LVPF composites. It can deliver a capacity of 154, 145, and 110 mAh g^{-1} at rates of 0.5, 1, and 5 C, respectively. However, the electrochemical performance, especially the rate performance of the LFP−LVPF composites, is still considerably worse than that of the LVP−LFP−LVPF composites in this study. Thus, we concluded that LVP can improve the rate performance in composites. Moreover, the cycle performance of the LFP−LVP−LVPF composites is better than that of the LFP−LVP composites but is slightly worse than that of the LVP−LVPF composites. These results can be attributed to the LVPF mass reduction in the LFP−LVP−LVPF composites compared with the LVP−LVPF composites.

From the above comparative investigation of the phosphate-based composite materials of LVP−LVPF, LFP−LVP, and LFP−LVP−LVPF, the findings indicate that LFP has a substantial effect on composite capacity. And, LVPF can improve cycle performance. In addition, LVP can produce

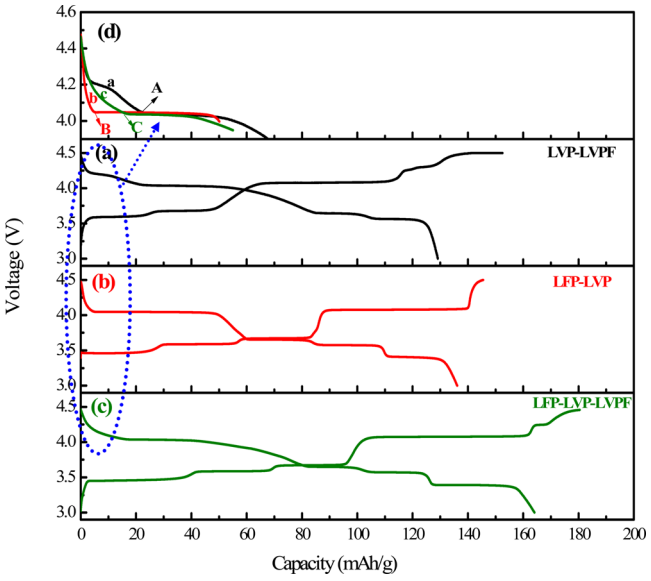

Figure 3. Charge/discharge performance for (a) LVP−LVPF; (b) LFP−LVP; and (c) LFP−LVP−LVPF; (d) a zoom on the low-discharge capacity region for LVP−LVPF, LFP−LVP, and LFP−LVP−LVPF composites.

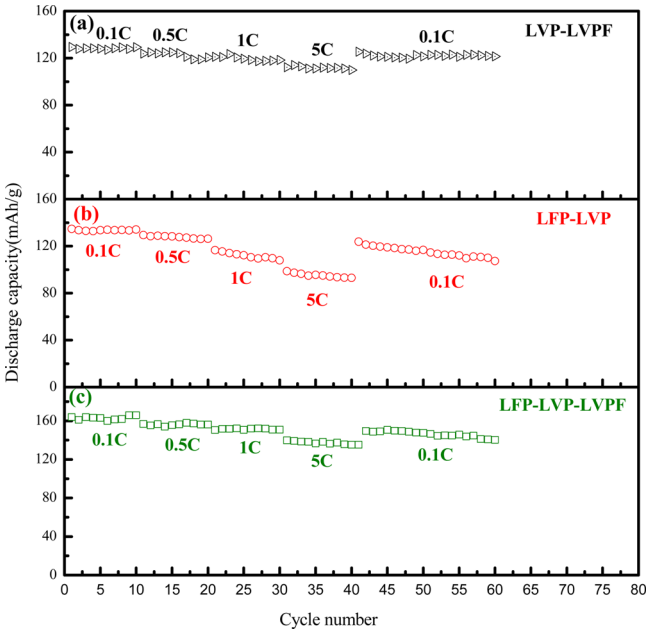

Figure 4. Cycle performance of (a) LVP−LVPF; (b) LFP−LVP; and (c) LFP−LVP−LVPF.

some synergy to improve the rate performance and supply 3D fast ion transport, which overcomes the olivine 1D ion conductivity challenge.[14,22,38] To obtain the best performance of the composites, the content of each phase in the composite materials must be regulated, and their advantages must be fully utilized.

Figure 5a shows the CV curves of the LVP−LVPF composites. Five oxidation peaks and four reduction peaks are found within the potential range of 3.0−4.5 V. These peaks correspond to 3.6 V/3.53 V, 3.7 V/3.63 V, and 4.1 V/4.01 V for LVP and 4.27 V and 4.35 V/4.16 V for LVPF, which are consistent with the charge/discharge curves (Figure 3a). Figure 5b shows the CV curves of the LFP−LVP composites. Redox

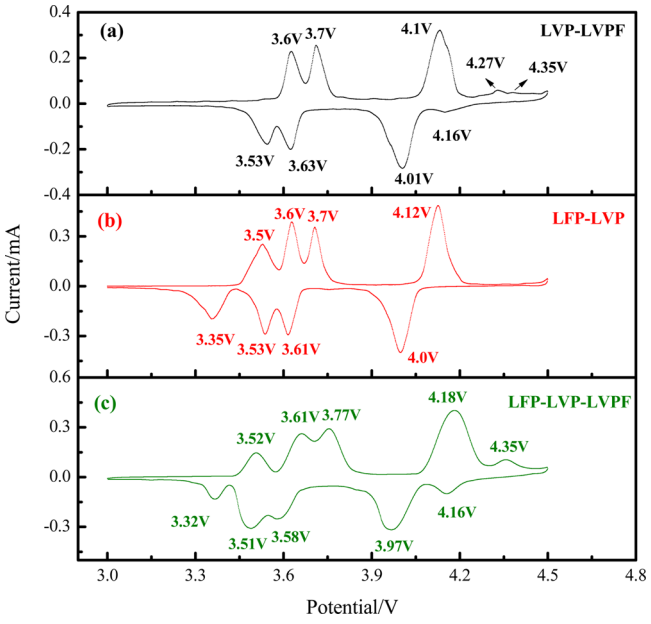

Figure 5. Cyclic voltammogram recorded for (a) LVP−LVPF; (b) LFP−LVP; and (c) LFP−LVP−LVPF at a scan rate of 0.1 mV s^{-1} in the potential range of 3.0−4.5 V.

peaks for both $LiFePO_4$ (3.5 V/3.35 V) and $Li_3V_2(PO_4)_3$ (3.6 V/3.53 V, 3.7 V/3.61 V, and 4.12 V/4.0 V) are consistent with the charge/discharge curves of the LFP−LVP composites (Figure 3b). Figure 5c shows the CV curves of the LFP−LVP−LVPF composites. The redox peaks for LVP are 3.61 V/3.51 V, 3.77 V/3.58 V, and 4.18 V/3.97 V, and that for LFP is 3.52 V/3.32 V. The peak at 4.35 V/4.16 V corresponds to the LVPF redox peak, which is different from that of the LVP−LVPF composites (Figure 5a) but consistent with the charge/discharge curves of the LFP−LVP−LVPF composites (Figure 3c).

The electrochemical impedance spectroscopy (EIS) measurements are performed for the LVP−LVPF, LFP−LVP, and LFP−LVP−LVPF composites, and the Nyquist plots are shown in Figure6a. Both spectra show typical Nyquist characteristics. The solution resistance is given by the intercept impedance at high frequencies. The semicircle in the high-middle frequency region refers to the charge transfer process (Rct). The inclined line in the low frequency region is associated with the Warburg impedance. The diagrams are refined using the Zview program, and the equivalent circuit is shown in Figure 6b. The experimental data fit well with the equivalent circuit. Table 3 shows the parameters of the equivalent circuit. The charge-transfer impedances of the LVP−LVPF, LFP−LVP, and LFP−LVP−LVPF composites are about 67.8, 138.5, and 113 Ω, respectively. On the basis of the study of Chen et al.,[42] Rct is the main contributor to cathode impedance. Consequently, low charge-transfer impedances correspond to good ion transport kinetics. The EIS results are consistent with the results of electrochemical performance analysis.

4. CONCLUSIONS

$Li_3V_2(PO_4)_3$−$LiVPO_4F$, $LiFePO_4$−$Li_3V_2(PO_4)_3$, and $LiFePO_4$−$Li_3V_2(PO_4)_3$−$LiVPO_4F$ composites are synthesized through mechanically activated chemical reduction followed by annealing. The XRD patterns and TEM images show that different phases can coexist in grain of the composites. From

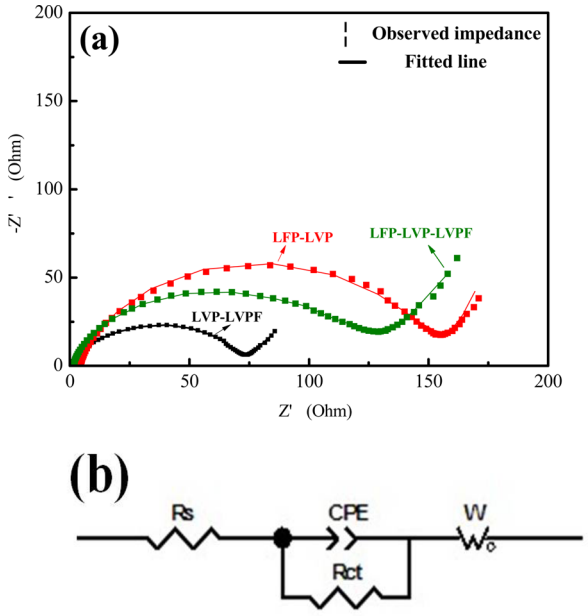

Figure 6. (a) Electrochemical impedance spectra (EIS) curves for LVP–LVPF, LFP–LVP, and LFP–LVP–LVPF at the frequency from 0.1 Hz to 100 KHz. (b) Equivalent circuit used for fitting the experimental parameters of EIS.

Table 3. Solution Transfer Resistance (R_s) and Charge Transfer Resistance (R_{ct}) Generated from the Equivalent Circuit Fitting

sample	R_s (Ω)	R_{ct} (Ω)
LVP–LVPF	0.066	67.8
LFP–LVP	0.67	138.5
LFP–LVP–LVPF	0.34	113

the comparative investigation on electrochemical performance for the three samples, the findings indicate that LFP has a significant effect on the capacity of composites, LVPF can improve cycle performances, LVP can produce some synergy to improve the rate performance, and the LFP–LVP–LVPF composites have excellent electrochemical performance. The proposed strategy is a good way to obtain composite cathode materials with excellent electrochemical performance by regulating the contents of each phase in the composite materials and fully utilizing their advantages.

AUTHOR INFORMATION

Corresponding Author

*Tel.:+86-731-88836357. E-mail: jczheng@csu.edu.cn.

Author Contributions

†These authors (Jun-chao Zheng and Ya-dong Han) contributed equally to this work and should be considered cofirst authors.

Notes

The authors declare no competing financial interest.

ACKNOWLEDGMENTS

This study was supported by National Natural Science Foundation of China (Grant No. 51302324).

REFERENCES

(1) Roy, R.; Hoffman, D. W.; Komarneni, S. A New Class of Materials: Phases in the System Al_2O_3-SiO_2. *J. Am. Ceram. Soc.* **1984**, *67*, 468–471.
(2) Bergman, D. J. Exactly Solvable Microscopic Geometries and Rigorous Bounds for The Complex Dielectric Constant of A Two-component Composite Material. *Phys. Rev. Lett.* **1980**, *44*, 1285–1287.
(3) Milton, G. W. Bounds on The Complex Dielectric Constant of A Composite Material. *Appl. Phys. Lett.* **1980**, *37*, 300–302.
(4) Meo, M.; Polimeno, U.; Zumpano, G. Detecting Damage In Composite Material Using Nonlinear elastic Wave Spectroscopy Methods. *Appl. Compos. Mater.* **2008**, *15*, 115–126.
(5) Zhu, X.; Zhu, Y.; Murali, S. Nanostructured Reduced Graphene Oxide/Fe_2O_3 Composite As A High-performance Anode Material for Lithium Ion Batteries. *ACS Nano* **2011**, *5*, 3333–3338.
(6) Derrien, G.; Hassoun, J.; Panero, S. Nanostructured Sn-C Composite As an Advanced Anode Material in High-Performance Lithium-Ion Batteries. *Adv. Mater.* **2007**, *19*, 2336–2340.
(7) Morita, T.; Takami, N. Nano Si Cluster-SiO_x-C Composite Material as High-Capacity Anode Material for Rechargeable Lithium Batteries. *J. Electrochem. Soc.* **2006**, *153*, A425–A430.
(8) Thackeray, M. M.; Johnson, C. S.; Vaughey, J. T. Advances in Manganese-oxide 'Composite' Electrodes for Lithium-Ion Batteries. *J. Mater. Chem.* **2005**, *15*, 2257–2267.
(9) Li, H.; Huang, X.; Chen, L. A High Capacity Nano Si Composite Anode Material for Lithium Rechargeable Batteries. *Electrochem. Solid-State Lett.* **1999**, *2*, 547–549.
(10) Wen, Z. S.; Yang, J.; Wang, B. F. High Capacity Silicon/Carbon Composite Anode Materials for Lithium Ion Batteries. *Electrochem. Commun.* **2003**, *5*, 165–168.
(11) Liu, J.; Xia, H.; Xue, D. Double-shelled Nanocapsules of V_2O_5-Based Composites As High-performance Anode and Cathode Materials for Li Ion Batteries. *J. Am. Chem. Soc.* **2009**, *131*, 12086–12087.
(12) Zhang, B.; Shen, C.; Zheng, J. Synthesis and Characterization of a Multi-Layer Core-Shell Composite Cathode Material $LiVOPO_4$-$Li_3V_2(PO_4)_3$. *J. Electrochem. Soc.* **2014**, *16*, A748–A752.
(13) Huang, Y. H.; Park, K. S.; Goodenough, J. B. Improving Lithium Batteries by Tethering Carbon-coated $LiFePO_4$ to Polypyrrole. *J. Electrochem. Soc.* **2006**, *153*, A2282–A2286.
(14) Yuan, L. X.; Wang, Z. H.; Zhang, W. X. Development and Challenges of $LiFePO_4$ Cathode Material for Lithium-Ion Batteries. *Energy Environ. Sci.* **2011**, *4*, 269–284.
(15) Andersson, A. S.; Thomas, J. O.; Kalska, B. Thermal Stability of $LiFePO_4$-Based Cathodes. *Electrochem. Solid-State Lett.* **2000**, *3*, 66–68.
(16) Gaubicher, J.; Wurm, C.; Goward, G. Rhombohedral Form of $Li_3V_2(PO_4)_3$ As a Cathode in Li-ion Batteries. *Chem. Mater.* **2000**, *12*, 3240–3242.
(17) Martha, S. K.; Markovsky, B.; Grinblat, J. $LiMnPO_4$ As an Advanced Cathode Material for RechargeableLithium Batteries. *J. Electrochem. Soc.* **2009**, *156*, A541–A552.
(18) Barker, J.; Gover, R. K. B.; Burns, P. A Symmetrical Lithium-Ion Cell Based on Lithium Vanadium Fluorophosphates, $LiVPO_4F$. *Electrochem. Solid-State Lett.* **2005**, *8*, A285–A287.
(19) Barker, J.; Gover, R. K. B.; Burns, P. Structural and Electrochemical Properties of Lithium Vanadium Fluorophosphate, $LiVPO_4$ F. *J. Power Sources* **2005**, *146*, 516–520.
(20) Ren, M. M.; Zhou, Z.; Gao, X. P. Core-shell $Li_3V_2(PO_4)_3$/C Composites As Cathode Materials for Lithium-Ion Batteries. *J. Phys. Chem. C* **2008**, *112*, 5689–5693.
(21) Chen, Y.; Zhao, Y.; An, X. Preparation and Electrochemical Performance Studies on Cr-doped $Li_3V_2(PO_4)_3$ As Cathode Materials for Lithium-Ion Batteries. *Electrochim. Acta* **2009**, *54*, 5844–5850.
(22) Hu, Y. S.; Guo, Y. G.; Dominko, R. Improved Electrode Performance of Porous $LiFePO_4$ Using RuO_2 As an Oxidic Nanoscale Interconnect. *Adv. Mater.* **2007**, *19*, 1963–1966.

(23) L, Y.; Zhou, Z.; Gao, X. P. A Novel Sol-Gel Method to Synthesize Nanocrystalline $LiVPO_4F$ and Its Electrochemical Li Intercalation Performances. *J. Power Sources* **2006**, *160*, 633−637.
(24) Croce, F.; d'Epifanio, A.; Hassoun, J. A Novel Concept for The Synthesis of An Improved $LiFePO_4$ Lithium Battery Cathode. *Electrochem. Solid-State Lett.* **2002**, *5*, A47−A50.
(25) Fergus, J. W. Recent Developments in Cathode Materials for Lithium Ion Batteries. *J. Power Sources* **2010**, *195*, 939−954.
(26) Li, X. L.; Kang, F. Y.; Bai, X. D.; Shen, W. C. A Novel Network Composite Cathode of $LiFePO_4$/Multiwalled Carbon Nanotubes with High Rate Capability for Lithium Ion Batteries. *Electrochem. Commun.* **2007**, *9*, 663−666.
(27) Wang, G. X.; Yang, L.; Chen, Y.; Wang, J. Z.; Bewlay, S.; Liu, H. K. An Investigation of Polypyrrole-$LiFePO_4$ Composite Cathode Materials for Lithium-Ion Batteries. *Electrochim. Acta* **2005**, *50*, 4649−4654.
(28) Yuan, L. X.; Wang, Z. H.; Zhang, W. X.; Hu, X. L.; Chen, J. T.; Huang, Y. H. Development and Challenges of $LiFePO_4$ Cathode Material for Lithium-Ion Batteries. *Energy Environ. Sci.* **2010**, *4*, 269−284.
(29) Zheng, J.; Li, X.; Wang, Z. Characteristics of $xLiFePO_4{\cdot}yLi_3V_2(PO_4)_3$ Electrodes for Lithium Batteries. *Ionics* **2009**, *15*, 753−759.
(30) Wu, L.; Lu, J.; Zhong, S. Studies of $xLiFePO_4{\cdot}yLi_3V_2(PO_4)_3$/C Composite Cathode Materials with High Tap Density and High Performance Prepared by Sol Spray Drying Method. *J. Solid State Electrochem.* **2013**, *17*, 1−7.
(31) Zhang, B.; Zheng, J.; Yang, Z. Structural Properties of Composite Cathode Material $LiFePO_4$-$Li_3V_2(PO_4)_3$. *Ionics* **2011**, *17*, 859−862.
(32) Guo, Y.; Huang, Y.; Jia, D. Preparation and Electrochemical Properties of High-capacity $LiFePO_4$-$Li_3V_2(PO_4)_3$/C Composite for Lithium-Ion Batteries. *J. Power Sources* **2014**, *246*, 912−917.
(33) Wang, J.; Wang, Z.; Li, X. $xLi_3V_2(PO_4)_3{\cdot}LiVPO_4F$/C Composite Cathode Materials for Lithium Ion Batteries. *Electrochim. Acta* **2013**, *87*, 224−229.
(34) Lin, Y. C.; Ting-Kuo; Fey, G.; Wu, P. J. Synthesis and Electrochemical Properties of $xLiFePO_4{\cdot}(1\text{-}x)LiVPO_4F$ Composites Prepared by Aqueous Precipitation and Carbothermal Reduction. *J. Power Sources* **2013**, *244*, 1−9.
(35) Barker, J.; Gover, R. K. B.; Burns, P. Performance Evaluation of Lithium Vanadium Fluorophosphate in Lithium Metal and Lithium-Ion Cells. *J. Electrochem. Soc.* **2005**, *152*, A1776−A1779.
(36) Yin, S. C.; Strobel, P. S.; Grondey, H. $Li_{2.5}V_2(PO_4)_3$: A Room-temperature Analogue to the Fast-ion Conducting High-temperature γ-phase of $Li_3V_2(PO_4)_3$. *Chem. Mater.* **2004**, *16*, 1456−1465.
(37) Lee, S.; Park, S. S. Atomistic Simulation Study of Monoclinic $Li_3V_2(PO_4)_3$ as a Cathode Material for Lithium Ion Battery: Structure, Defect Chemistry, Lithium Ion Transport Pathway, and Dynamics. T. *J. Phys. Chem. C* **2012**, *116*, 25190−25197.
(38) Davis, L. J. M.; Heinmaa, I.; Goward, G. R. Study of Lithium Dynamics in Monoclinic $Li_3Fe_2(PO_4)_3$ using 6 Li VT and 2D Exchange MAS NMR Spectroscopy. *Chem. Mater.* **2009**, *22*, 769−775.
(39) Kim, G. H.; Kim, J. H.; Myung, S. T. Improvement of High-Voltage Cycling Behavior of Surface-Modified $Li[Ni_{1/3}Co_{1/3}Mn_{1/3}]O_2$ Cathodes by Fluorine Substitution for Li-Ion Batteries. *J. Electrochem. Soc.* **2005**, *152*, A1707−A1713.
(40) Amatucci, G. G.; Pereira, N.; Zheng, T.; Tarascon, J. M. Failure Mechanism and Improvement of the Elevated Temperature Cycling of $LiMn_2O_4$ Compounds Through the Use of the $LiAl_xMn_{2-x}O_{4-z}F_z$ Solid Solution. *J. Electrochem. Soc.* **2001**, *148*, A171−A182.
(41) Liao, X. Z.; He, Y. S.; Ma, Z. F.; Zhang, X. M.; Wang, L. Effects of Fluorine Substitution on the Electrochemical Behavior of $LiFePO_4$/C Cathode Materials. *J. Power Sources* **2007**, *174*, 720−725.
(42) Chen, C. H.; Liu, J.; Amine, K. Symmetric Cell Approach and Impedance Spectroscopy of High Power Lithium-Ion Batteries. *J. Power Sources* **2001**, *96*, 321−328.